

# Molecular Dynamics Study of the Sonic Horizon of Microscopic Laval Nozzles

Helmut Ortmayer<sup>1,2</sup>, Robert E. Zillich<sup>1</sup>

<sup>1</sup>*Institute for Theoretical Physics, Johannes Kepler University, Altenbergerstrasse 69, 4040 Linz, Austria and*

<sup>2</sup>*Primetals Technologies Austria GmbH, Turmstrasse 44, A-4031 Linz, Austria*

A Laval nozzle can accelerate expanding gas above supersonic velocities, while cooling the gas in the process. This work investigates this process for microscopic Laval nozzles by means of non-equilibrium molecular dynamics simulations of stationary flow, using grand canonical Monte-Carlo particle reservoirs. We study the expansion of a simple fluid, a mono-atomic gas interacting via a Lennard-Jones potential, through an idealized nozzle with atomically smooth walls. We obtain the thermodynamic state variables pressure, density, and temperature, but also the Knudsen number, speed of sound, velocity, and the corresponding Mach number of the expanding gas for nozzles of different sizes. We find that the temperature is well-defined in the sense that the each velocity components of the particles obey the Maxwell-Boltzmann distribution, but it is anisotropic, especially for small nozzles. The velocity auto-correlation function reveals a tendency towards condensation of the cooled supersonic gas, although the nozzles are too small for the formation of clusters. Overall we find that microscopic nozzles act qualitatively like macroscopic nozzles in that the particles are accelerated to supersonic speeds while their thermal motion relative to the stationary flow is cooled. We find that, like macroscopic Laval nozzles, microscopic nozzles also exhibit a sonic horizon, which is well-defined on a microscopic scale. The sonic horizon is positioned only slightly further downstream compared to isentropic expansion through macroscopic nozzles, where the sonic horizon is situated in the most narrow part. We analyze the sonic horizon by studying spacetime density correlations, i.e. how thermal fluctuations at two positions of the gas density are correlated in time and find that after the sonic horizon there are indeed no upstream correlations on a microscopic scale.

## I. INTRODUCTION

The Laval nozzle converts thermal kinetic energy into translational kinetic energy and was invented by Gustaf de Laval in 1888 for actuating steam turbines with steam accelerated by expansion. The goal was to achieve the highest possible velocity of an expanding gas, made possible with the convergent-divergent nozzle shape. The left panel of Fig. 1 schematically shows the cross section of such a nozzle. When the gas reaches the most narrow part, the nozzle throat, the flow can become supersonic. The surface where this happens is called sonic horizon (or acoustic horizon) [1, 2] because no information carried by sound waves can travel upstream through the sonic horizon.

The expansion of gas in a Laval nozzle has interesting thermodynamic properties. While the gas acceleration of macroscopic Laval nozzles is exploited for propulsion purposes in rocket engines, the temperature drop during expansion through a nozzle with a diameter in the tenth of  $\mu\text{m}$  range is exploited in supersonic jet spectroscopy to freeze out translational, rotational and vibrational degrees of freedom of molecules, leading to spectra that are not complicated by too many thermally populated excited states [3–6]. The studied molecules can be kept in a supercooled gas phase, far below the condensation temperature, with a high density compared to a conventionally cooled equilibrium vapor. Under appropriate conditions, weakly bound van der Waals cluster can be formed [7, 8]. The molecules of interest are typically co-expanded

with a noble gas. In case of  $^4\text{He}$  as carrier the cooling effect is also greatly enhanced by the unique quantum effects of  $^4\text{He}$  at low temperatures. Especially the helium-droplet beam technique takes additional advantage from the superfluidity of  $^4\text{He}$ [7–9]. The typical orifice used for molecular beams has only a convergent part and the divergent nozzle part is realized by the ambient pressure in the expansion chamber. During expansion the surrounding gas in the chamber provides a pressure boundary to the jet and the jet temperature itself keeps decreasing after exiting the orifice. [10].

Macroscopic Laval nozzles are well understood and can be approximately described by simple thermodynamic considerations, under assumptions that are reasonable for macroscopic nozzles: isentropic flow without dissipation (inviscid gas and smooth slip boundaries); the flow velocity  $v$  depends only on the position  $x$  along the axis of the nozzle; the nozzle cross section varies only gradually with  $x$ ; the flow is stationary; and continuum fluid dynamics is valid, i.e. each fluid element is in local thermodynamic equilibrium. Then the relative velocity change with  $x$  and the relative change of the cross section area  $A$  follow the simple relation [10]

$$\frac{dv}{v} = - \frac{1}{1 - \left(\frac{v}{c}\right)^2} \frac{dA}{A} \quad (1)$$

where  $c$  is the speed of sound, which can be expressed in terms of the isentropic or isothermic derivative of the pressure with respect to the density,

$$c = \sqrt{\left(\frac{\partial p}{\partial \rho}\right)_S} = \sqrt{\frac{c_p}{c_v} \left(\frac{\partial p}{\partial \rho}\right)_T} \quad (2)$$

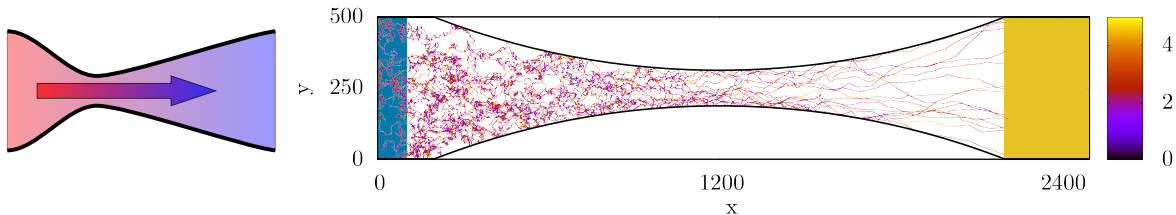


FIG. 1. Left: Cross section of a Laval nozzle with a convergent and divergent nozzle part. Indicated by the arrow and color is the flow direction and temperature decrease of the expanding gas.

Right: Molecular dynamics trajectories of 30 randomly chosen particles starting in the shaded area to the left. The average total particle number in the nozzle for this simulation is much larger, approx. 790000. The velocity of these particles is indicated by color. While the subsonic motion in the convergent part is dominated by random thermal motion, the supersonic motion of the particles in the divergent part is

where  $c_p$  and  $c_v$  is the heat capacity at constant pressure and volume, respectively. The ratio  $M = v/c$  is called Mach number, and  $M = 1$  defines the sonic horizon. The usual situation is a gas in a reservoir or a combustion chamber producing gas to the left in our figures of the nozzle. Hence the flow velocity is small when it enters the nozzle, in particular it is subsonic,  $M < 1$ . Eq. (1) tells us that, with decreasing cross section  $A$  (e.g. moving downstream in the convergent part), the flow velocity  $v$  must increase. In the nozzle throat, i.e. where  $A$  has a minimum and  $dA = 0$ ,  $v$  either stays below  $M$ , in which case  $v$  must decelerate in the divergent part. Or the gas flow attains  $M = 1$  in the nozzle throat, and then accelerates further in the divergent part (if the pressure difference between inlet and outlet is large enough). Hence for supersonic flow,  $v$  increases with *increasing*  $A$ . Note that Eq. (1) implies that the transition to supersonic flow can happen only where the cross section area has a minimum.

The goal of this work is to understand the physics of microscopic Laval nozzles on the nanoscale of the atoms of the gas flowing through a constriction which is only nanometers wide. We want to answer the following questions: How do the transport properties of a Laval nozzle depend on its size, and does it even have the typical characteristic of a convergent-divergent nozzle, i.e. converting thermal energy into translational energy? If yes, how efficiently does a nanoscale Laval nozzle cool the expanding gas? Do we obtain supersonic flow? Is there a well-defined sonic horizon, and if yes, where in the nozzle is it located? Is there even local thermodynamic equilibrium such that we can define a local speed of sound and thus can speak of a sonic horizon and supersonic flow? Since we are interested in the fundamental mechanism of a microscopic Laval nozzle we study a rather idealized nozzle with atomically flat surfaces corresponding to slip boundaries. This simplifies the problem since it eliminates the boundary layer close to the nozzle walls. Boundary effects are of course essential in a real microscopic nozzle, and they would be easy to model with rough walls, but they would complicate the analysis and interpretation of our results.

A common method to study microscopic nozzles is

the direct simulation Monte Carlo (DSMC) method [11–14], which solves the Boltzmann equation. However, we want to make as few approximations as possible, apart from the idealization of a atomically smooth nozzle walls. Therefore we use molecular dynamics (MD) simulations, which accounts for each atom or molecule of the gas, and collisions are described by realistic intermolecular interactions. Atomistic (MD) simulations have been shown to be useful for the understanding of fluid dynamic phenomena [15–22]. The only underlying assumption of the MD method is that quantum physics plays no role and classical mechanics is sufficient. This is usually a valid assumption, with the exception of expansion of  $^4\text{He}$  under conditions where the  $^4\text{He}$  gas cools to superfluid nanodroplets[23].

Because of the non-equilibrium nature of this expansion process through a Laval nozzle we perform non-equilibrium MD (NEMD) simulations [24]. The right panel of Fig. 1 shows the trajectories 30 randomly chosen particles of a simulation in a convergent-divergent nozzle that contained on average about 790000 particles. The speed of the particles is color-coded. Fig. 1 gives an impression how a Laval nozzle converts thermal energy (temperature) to ordered translation energy: close to the inlet the motion is predominantly thermal; close to the outlet the velocities are higher and tend to point in  $x$ -direction, but the temperature, i.e. the kinetic energy after subtracting the flow velocity, is in fact much lower as our results will show. Averaging over all particles and over time leads to the thermodynamic notion of a gas that accelerates and cools as it expands through the nozzle.

With MD we can obtain, with microscopic resolution, both thermodynamic quantities like temperature, pressure, or density, and microscopic quantities like the velocity autocorrelation function VACF, velocity distribution, or density fluctuation correlations: we will investigate whether the expanding gas has a well-defined temperature, characterized by an isotropic Maxwell-Boltzmann distribution of the thermal particle velocities. The VACF exhibits features related to the metastability of the accelerated gas cooled below condensation temperature. We

calculate spatio-temporal density auto-correlations, i.e. correlations between fluctuations of the density at different times and different locations, to study the propagation of information upstream and downstream and pinpoint the location of the sonic horizon (if it exists). In a macroscopic nozzle, upstream propagation of information carried by density fluctuations is not possible in the supersonic region. On the microscopic scale, e.g. on the scale of the mean free path of the atoms, a unidirectional information flow is not so obvious. For instance, if we assume a Maxwell-Boltzmann distribution of random particle velocities, fast particles from the tail of the distribution could carry information upstream.

We remark that, in a seminal paper by W. G. Unruh et al. [1], a mathematical analogue between the black hole evaporation by Hawking radiation and the fluid mechanical description of a sonic horizon is found. This analogue has brought significant attention to sonic horizons [2, 25–28], but in this work we will not study analog Hawking radiation.

## II. MOLECULAR DYNAMICS SIMULATION OF EXPANSION IN LAVAL NOZZLE

The gas flow through the microscopic Laval nozzle is simulated with the molecular dynamics (MD) method which solves Newton’s equation of motion for all particles of the gas. Unlike in continuum fluid dynamics, which solves the Navier-Stokes equation, MD contains thermal fluctuations of the pressure and density, also in equilibrium. Furthermore, unlike the continuum description, MD does not assume local thermodynamic equilibrium, which may not be fulfilled in a microscopic nozzle.

The price for an accurate atomistic description afforded by MD simulations is a high computational cost compared to Navier-Stokes calculations or DSMC simulations. In the present case, we simulate up to several hundred thousand particles. Larger MD simulations are possible, but our focus is the microscopic limit of a Laval nozzles on the nanometer scale. A challenge for MD is to implement effective reservoirs to maintain a pressure differential for a steady flow between inlet and outlet of the nozzle. An actual reservoir large enough to maintain its thermodynamic state during the MD simulation would be prohibitively computationally expensive. We approximate these reservoirs by defining small inlet and outlet regions where we perform a hybrid MD and MC Monte-Carlo simulation (GCMC) [29], with grand canonical Monte-Carlo exchange of particles [30]. As the name implies, this method simulates a grand canonical ensemble for a given chemical potential  $\mu$ , volume  $V$  and temperature  $T$  by inserting and removing particles. The nozzle itself is simulated in the microcanonical ensemble, i.e. energy is conserved. This ensemble represents a nozzle with perfect thermally insulating walls.

Fig. 2 shows the geometry of the nozzle simulated with the inlet and outlet colored in blue and yellow, respec-

tively, with the convergent-divergent nozzle in between. To keep the simulation simple and the computational effort in check we simulate a slit Laval nozzle, translationally invariant in  $z$ -direction (perpendicular to the plane of the figure) and realized with periodic boundaries in this direction. Since our focus is a microscopic understanding of supersonic flow and the sonic horizon, we simulate a nozzle with atomically smooth walls. Simulating rough walls would have significantly complicated the analysis of the flow, because of the nontrivial spatial dependence of the flow field in the direction perpendicular to the general flow direction, requiring significantly longer simulations to resolve all measured quantities in both  $x$  and  $y$  direction. In a smooth-walled nozzle, we can restrict ourselves to studying only the  $x$ -dependence of the quantities of interest.

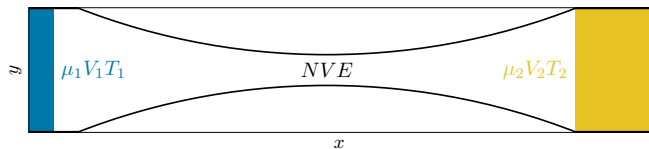


FIG. 2. Geometry of a slit Laval nozzle with the convergent and divergent part in the  $xy$ -plane. The nozzle walls are two cylinders. In the  $z$ -direction out of the plane, the nozzle is translationally invariant, realized with periodic boundary conditions. Particle insertion is done by grand canonical Monte Carlo insertion and deletion [29, 30] on the left side (blue) in the  $\mu_1 V_1 T_1$  ensemble. The nozzle region shown in white with the convergent end divergent boundaries is simulated in the microcanonical ensemble. Particle deletion is done on the right side (yellow) in a  $\mu_2 V_2 T_2$  ensemble.

The gas particles are atoms interacting via a pair-wise Lennard-Jones (LJ) potential. Thus we simulate the expansion of a noble gas through the nozzle. Molecules with vibrational and rotational degrees of freedom seeded into the noble gas would be an interesting subject for further investigation, but this exceeds the scope of this work. The (LJ) potential between a pair of particles with distance  $r$  is given by

$$V_{LJ}(r) = 4\epsilon \left[ \left( \frac{\sigma}{r} \right)^{12} - \left( \frac{\sigma}{r} \right)^6 \right] \quad (3)$$

The smooth walls are also modelled via a (LJ) potential with,

$$V_{LJ}(s) = 4\epsilon \left[ \left( \frac{\sigma}{s} \right)^{12} - \left( \frac{\sigma}{s} \right)^6 \right] \quad (4)$$

where  $s$  is the normal distance between atom and wall.

We use the common reduced units for simulations of LJ particles if not otherwise stated, see table I. Thus with the atom mass  $m$ , and the LJ parameters  $\sigma$  and  $\epsilon$  for a specific noble gas, the results can be converted from reduced units to physical units.

Atoms are inserted and deleted in the inlet (blue) and outlet (yellow) by running the MD simulation in

TABLE I. Conversion to dimensionless reduced units (\*) used in this work.

Quantity	reduced units
Distance	$x^* = x/\sigma$
Time	$t^* = t \sqrt{\frac{\epsilon}{m^* \sigma^2}}$
Energy	$E^* = E/\epsilon$
Velocity	$v^* = vt^*/\sigma$
Temperature	$T^* = T k_B/\epsilon$
Pressure	$P^* = P \frac{\sigma^3}{\epsilon}$
Density	$\rho^* = \rho \sigma^3$

these regions as a hybrid (GCMC) simulation [29]. The two grand canonical ensembles are characterized by their chemical potential, the volume, and the temperature,  $(\mu_1, V_1, T_1)$  and  $(\mu_2, V_2, T_2)$ , respectively. A proper choice of these thermodynamic variables ensures that on average, an excess of particles are inserted in the inlet and particle are eliminated in the outlet, such that a stationary gas flow is established after equilibration. There are alternative insertion method, such as the insertion-deletion method, where the mass flow is specified [31].

The temperature and chemical potential of the inlet reservoir is set to  $T_1 = 2.0$  and  $\mu_1 = -32$ , which would correspond to a density  $\rho_1 = 0.86$  and ensures that the pressure is not too high and the LJ particles remain in the gas phase. The particle insertion region in the nozzle is not in equilibrium with the grand canonical reservoir defining the  $(\mu_1, V_1, T_1)$  ensemble, because the inlet volume is not closed on the side facing the nozzle. The outflow must be compensated by additional insertions, which makes the insertion rate higher than the elimination rate. Indeed we observed that the average density in the insertion region is approximately half the density  $\rho_1$ . Also the temperature in the inlet region is lower than the set value  $T_1 = 2.0$ . The resulting pressure in the insertion region is  $p \approx 0.06$  in our reduced units. For Argon with  $\epsilon = 1.65 \cdot 10^{-21}$  J and  $\sigma = 3.4 \text{ \AA}$  [32] this translates to a temperature of  $T = 179\text{K}$  and a pressure  $p \approx 2.5 \cdot 10^6$  Pa in SI units. This is in the pressure range for molecular beam spectroscopy experiments [4].

The inlet conditions will converge to the specified reservoir variables if the number of GCMC moves is significantly larger than the number of MD moves, or if the size of the inlet region is increased; both increases computational cost. Alternatively, the inlet conditions may be matched to the desired pressure and temperature by fine-tuning the reservoir variables and running many equilibration simulations, which again requires a high computational effort. In this work we refrain from perfectly controlling the thermodynamic state of the inlet although it leads to effectively different inlet conditions in differently sized nozzles.

In the convergent-divergent part of the nozzle, between the two grand canonical ensembles, the atoms are prop-

agated in the microcanonical ensemble (i.e. energy and particle number are conserved), which is the most suitable ensemble for dynamic studies since the dynamics is not biased by a thermostat. Since we want to simulate expansion into vacuum, instead of choosing a very negative chemical potential, we simply set the pressure in the outlet to zero, such that particles entering the outlet region are deleted immediately.

For comparisons of different nozzle sizes, we scaled the slit nozzle in both  $x$  and  $y$  directions, while keeping the simulation box length  $z_{max}$  in the translationally invariant  $z$ -direction, perpendicular to the figure plane in Fig. 2, fixed. In the  $z$ -direction, we apply periodic boundary conditions. We compared different simulation box lengths  $z_{max}$  in  $z$ -direction to quantify unwanted finite size effects in  $z$ -direction. Ideally, we want to keep  $z_{max}$  larger than the mean free path. Especially for the dilute gas at the end of the divergent part, a sufficiently large  $z_{max}$  is required to avoid such effects. For most simulations, we found  $z_{max} = 86.18\sigma$  or  $z_{max} = 43.09\sigma$  to be adequate, as shown below.

We initialize the NEMD simulations with particles only in the inlet region. Equilibration is achieved when the total number of particle in the simulation does not increase anymore but just fluctuates about an average value. When this steady state is reached, we start measurements by averaging velocities, pressure, density etc.

The equilibrium equation of state for LJ particles is well known [33, 34]. The equation of state is not needed for the MD simulations, but it is helpful for the analysis of the results, particularly for the calculation of the speed of sound and the Mach number. Specifying the Mach number, temperature, or pressure rests on the assumption of local thermodynamic equilibrium, and thus on the validity of a local equation of state. In a microscopic nozzles where the state variables of the LJ gas changes on a very small temporal and spatial scale local thermodynamic equilibrium may be violated.

All simulation were done with the open source MD software LAMMPS [35, 36].

### III. THERMODYNAMIC PROPERTIES

In this section we present thermodynamic results of our molecular dynamic simulations of the expansion through slit Laval nozzles: density, pressure, temperature, and Mach number. We check whether a microscopic nozzle exhibits the transition to supersonic flow and where the sonic horizon is located in nozzles of various sizes, and we compare to ideal gas continuum dynamics. The atomistic NEMD simulation also allows us to investigate if the gas attains a local equilibrium everywhere in the nozzle, with a well-defined temperature.

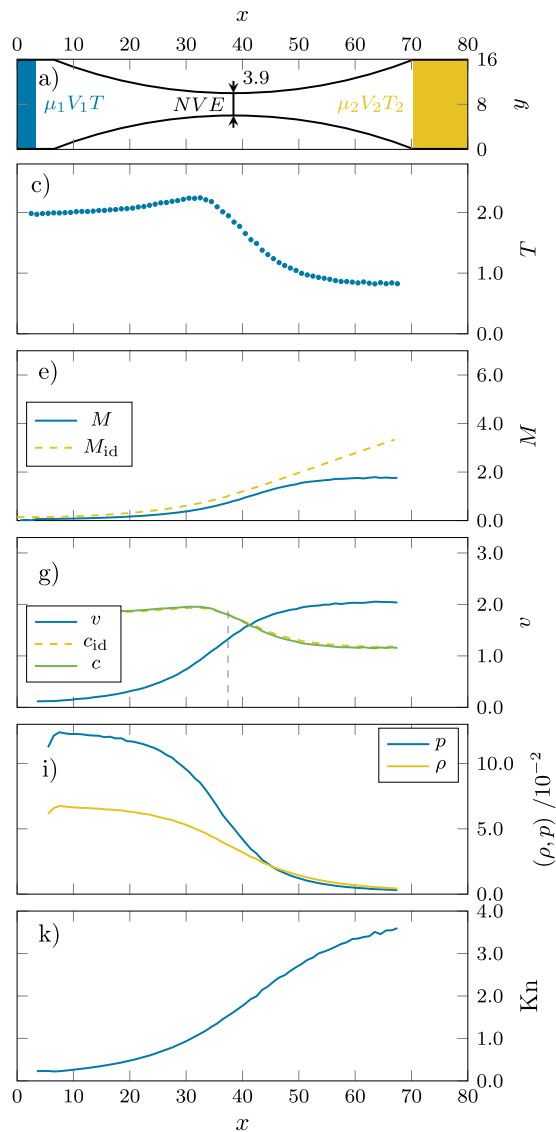


FIG. 3. Thermodynamic quantities for a nozzle with a throat width of only  $3.9\sigma$ . The figure shows in panel a) an overview of the nozzle in the  $x$ - $y$ -plane, in c) the temperature, in e) the Mach number  $M(x)$  and the ideal gas approximation for the Mach number  $M_{id}$ , in g) the ideal gas approximation of the speed of sound  $c_{id}$ , the speed of sound  $c$  obtained from the simulation and the averaged flow speed  $v$ , in i) the density  $\rho$  and pressure  $p$ , and in k) the Knudsen number. All quantities are shown as a function of the  $x$  position in the nozzle.

### A. Very small nozzle

Fig. 3 shows results for a very small Laval nozzle, with a throat width of only  $3.9\sigma$ , i.e. only a few atoms wide. Panel a) shows the nozzle geometry. The temperature is shown in panel c). The kinetic temperature is the thermal motion of the atoms after the flow velocity at  $\mathbf{r}$ ,

$\mathbf{v}(\mathbf{r})$  is subtracted

$$\frac{3}{2}k_B T = \sum_i \frac{m}{2} (\mathbf{v}_i - \mathbf{v}(\mathbf{r}_i))^2 \quad (5)$$

Unlike in equilibrium, the temperature in a non-equilibrium situation such as stationary flow varies spatially,  $T = T(\mathbf{r})$ , provided that local equilibrium is fulfilled. If there is no local equilibrium, there is no well-defined temperature. Although the right hand side of eq.(5) can still be evaluated, the notion of a “temperature” is meaningless if the thermal parts of the atom velocities do not follow a Maxwell-Boltzmann distribution. Here we assume that eq.(5) provides a well-defined local temperature  $T(x)$  at position  $x$  along the flow direction in our Laval nozzles. Further below we investigate whether this assumption is justified. The subtleties of the calculation of  $\mathbf{v}(\mathbf{r})$  and  $T(x)$ , and how to subtract the flow velocity from the particle velocities can be found in appendix C and D, respectively.

Fig. 3 shows that  $T(x)$  indeed drops after the gas passes the nozzle throat, but there is a small increase before it reaches the throat. We attribute this to the wall potential: the constriction is dominated by the attractive well of the LJ potential (4). The associated drop in potential energy is accompanied by an increase of the temperature, i.e. kinetic energy.

Panel g) shows the flow speed  $v(x) = |\mathbf{v}(x)|$ .  $v(x)$  increases monotonously over the whole length of the nozzle. For comparisons, we also show the speed of sound of the LJ gas  $c(x)$  and of the ideal gas  $c_{id}(x)$ , which are very similar, even in the convergent part where the density is higher. For a monatomic ideal gas, the speed of sound (2) becomes

$$c_{id}(x) = \sqrt{\frac{5}{3}k_B T(x)/m}. \quad (6)$$

The speed of sound  $c(x)$  of the LJ fluid is calculated from its equation of state given in Ref. [33] and the specific residual heat capacities [34], using the expression with the isothermal derivative in Eq. (2) and the values of  $\rho(x)$  and  $T(x)$  measured in the MD nozzle simulations.  $\rho(x)$  is shown in panel i), together with the pressure. The heat capacities  $c_p$  and  $c_v$  appearing in eq.(2) are also obtained from the equation of state of the LJ fluid. Note that applying the equation of state at position  $x$  in the nozzle again assumes local equilibrium, which is not necessarily true.

Panel e) shows the Mach number  $M(x)$  obtained from the simulation and the Mach number  $M_{id}(x)$  for an ideal gas continuum. For the ideal gas, we can derive from eq. (1) a relation between the cross section areas  $A(x)$  and Mach numbers  $M_{id}(x)$  at two different positions  $x_1$  and  $x_2$  in the nozzle [10]

$$\frac{A(x_1)}{A(x_2)} = \frac{M_{id}(x_2)}{M_{id}(x_1)} \left( \frac{1 + \frac{\gamma-1}{2} M_{id}^2(x_1)}{1 + \frac{\gamma-1}{2} M_{id}^2(x_2)} \right)^{\frac{\gamma+1}{2(\gamma-1)}} \quad (7)$$

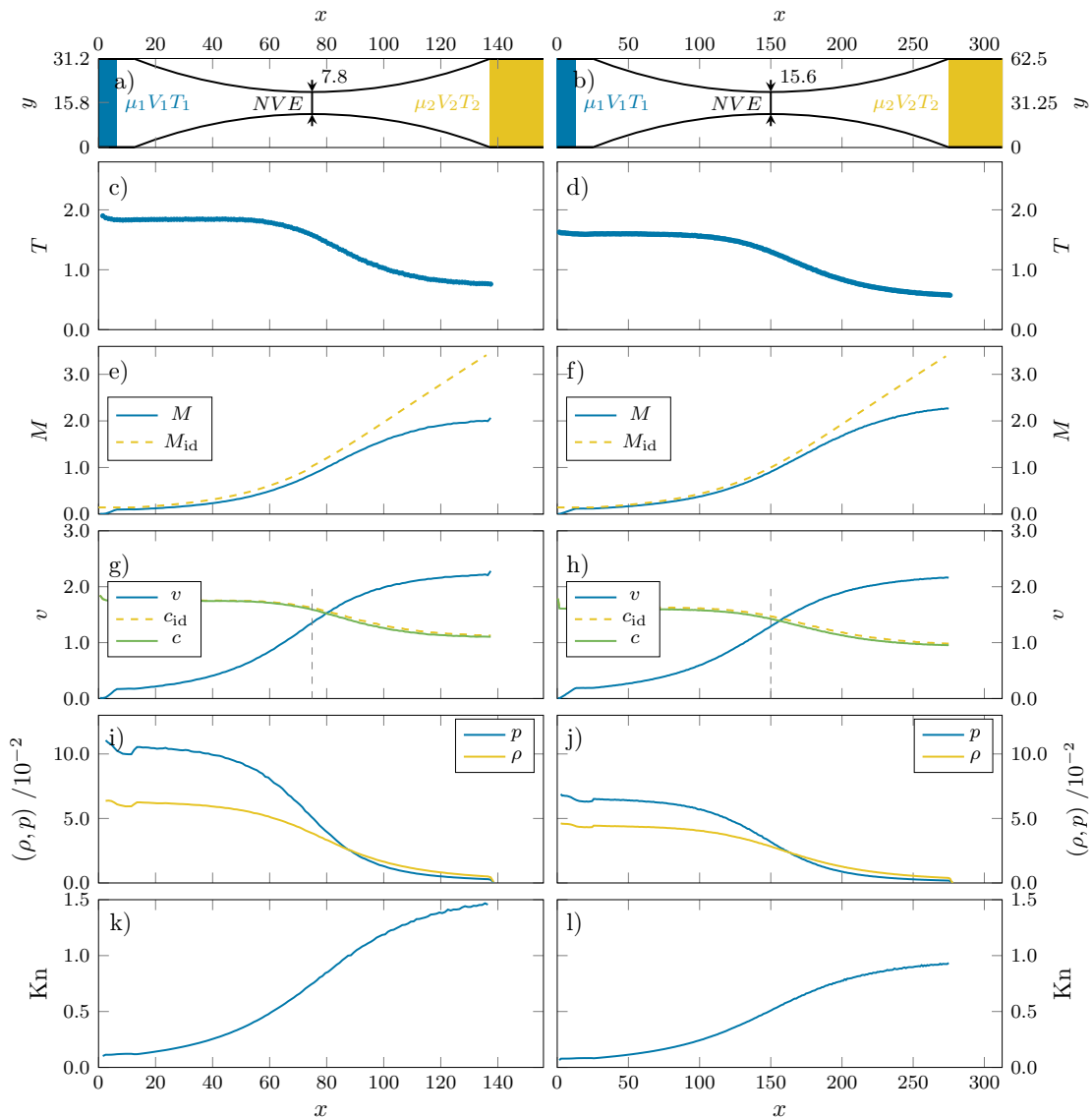


FIG. 4. Same as Fig.3 for a throat width of  $7.8\sigma$  (left column) and  $15.6\sigma$  (right column).

$M_{\text{id}}(x)$  can now be obtained by setting  $x_1 = x$  and  $x_2 = x_c$ , the position of the sonic horizon, where  $M_{\text{id}}(x_c) = 1$  by definition. Panel e) shows that the Mach number  $M(x)$  obtained from the simulation stays below the ideal gas approximation  $M_{\text{id}}(x)$ , with the difference growing in the divergent part of the nozzle. At the end of the nozzle  $M$  is approximately half the value of the ideal gas continuum approximation  $M_{\text{id}}$ . In particular, the sonic horizon predicted by the MD simulation is located *after* the throat of the nozzle, not at the point of smallest cross section predicted by the continuum description of isentropic flow, see eq. (1).

The Knudsen number is a characteristic quantity for flow in confined geometries. It is the mean free path length  $\lambda$  divided by a characteristic length  $d$  of confine-

ment

$$\text{Kn}(x) = \frac{\lambda(x)}{d(x)} \quad (8)$$

In our slit Laval nozzle  $d(x)$  is the width at position  $x$ . We estimate the mean free path  $\lambda(x)$  using a hard sphere approximation [37]

$$\lambda(x) = \left( \sqrt{2} \rho(x) \pi \right)^{-1} \quad (9)$$

under the assumption of a Maxwell-Boltzmann distribution of the velocities which check to be fulfilled in the nozzle, see section IV A and Fig. 7. For  $\text{Kn} \ll 1$  the mean free path is much smaller than the nozzle width and a continuum description of the flow is appropriate. For  $\text{Kn} \approx 1$  or  $\text{Kn} \gg 1$  a continuum description is not

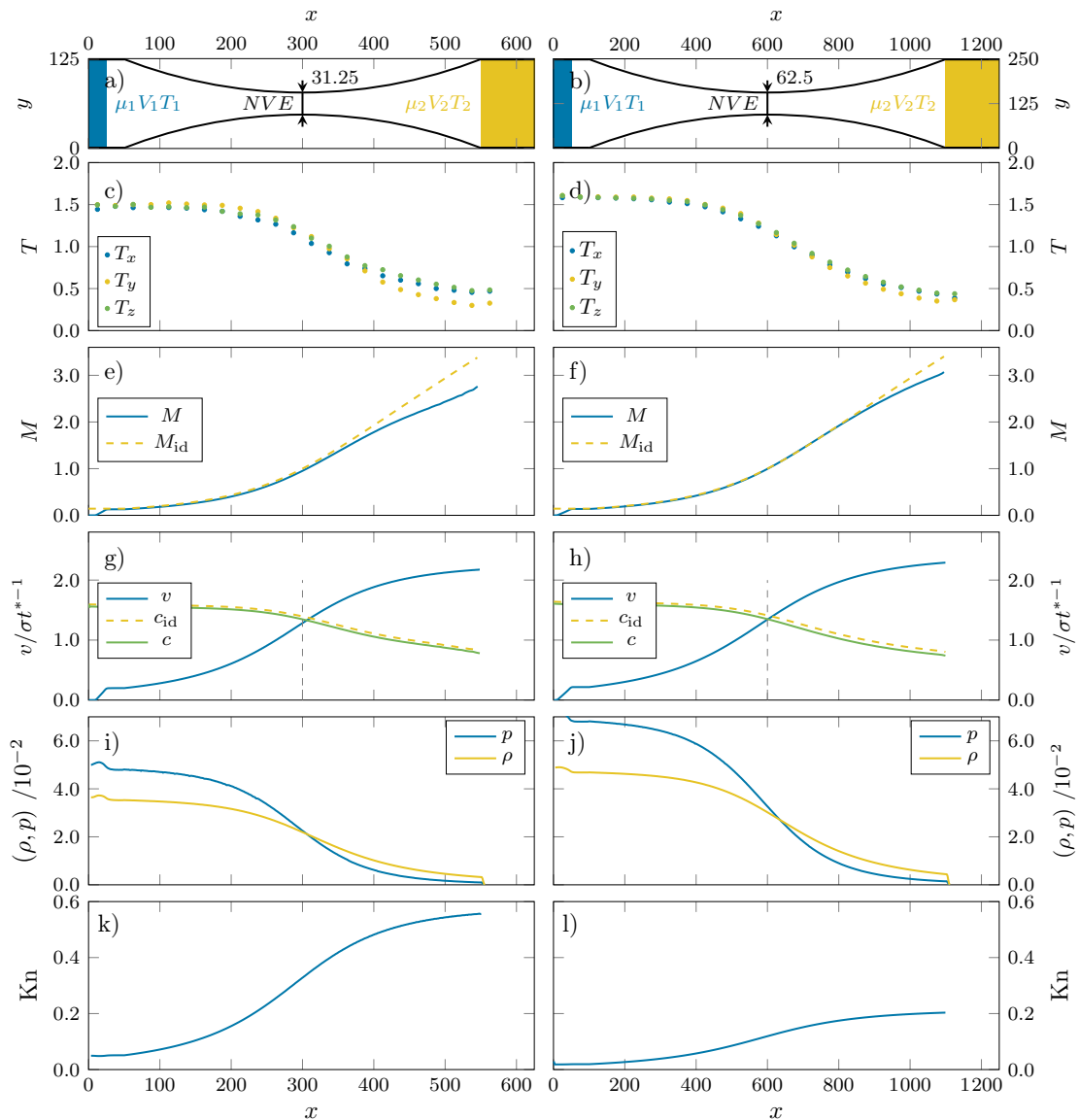


FIG. 5. Same as Fig.3 for a throat width of  $31.25\sigma$  (left column) and  $62.5\sigma$  (right column). The temperature is split into its contribution from motion in  $x$ ,  $y$  and  $z$  direction.

possible and the transport becomes partly ballistic. For the smallest nozzle results, the Knudsen number  $\text{Kn}(x)$  shown in panel k) in Fig. 3, is significantly larger than unity in the supersonic regime.

### B. Small nozzles

Fig. 4 shows results for two nozzles twice and four times as large as the smallest nozzle presented in Fig.3, with throat widths  $7.8\sigma$  and  $15.6\sigma$ , respectively. The small temperature increase seen for the smallest nozzle is not present anymore.  $T$  is almost constant in the convergent part and then decreases monotonously. Note that for each nozzle, the flow starts from slightly different ther-

modynamics conditions in the inlet region, for reasons explained above. As the nozzle size increases, the Mach number  $M$  reaches a higher value for the larger nozzle despite the slightly lower  $T$  in the inlet, and it follows the ideal gas approximation  $M_{\text{id}}$  more closely. The sonic horizon moves closer to the minimum of the cross section. Of course the Knudsen number  $\text{Kn}(x)$  is smaller for larger nozzles. Due to the wider nozzle throat, the pressure is significantly lower in the convergent part.

For Fig. 5, we increase the nozzle size again twofold and fourfold. We find the same trends as in Fig. 4. For the nozzle with throat width  $62.5\sigma$ , the Mach number  $M$  is close to the ideal gas approximation  $M_{\text{id}}$ .  $M$  falls below  $M_{\text{id}}$  only towards the end of the nozzle, where the collision rate presumably becomes too low for efficient

$d_m$	$\Delta x_c$	$\frac{\Delta x_c}{d_m}$
3.90	3.78	0.97
7.80	4.97	0.64
15.60	5.96	0.38
31.25	6.09	0.19
62.50	2.74	0.044

TABLE II. Downstream shift  $\Delta x_c$  of the sonic horizon with respect to the center position predicted by continuum fluid dynamics. Nozzles are characterized by the minimal width  $d_m$ . The right column shows the dimensionless difference in relation to nozzle size,  $\frac{\Delta x_c}{d_m}$ .

cooling. The sonic horizon is essentially in the center, indicated by the vertical dashed line.

For these two largest nozzles, we examined whether local equilibrium is fulfilled. The direction-dependent temperature, see appendix D, is shown in panel c) and d) of Fig. 5. The temperature is not quite isotropic, i.e. there is insufficient local equilibration between the motion in  $x$ -,  $y$ , and  $z$ -direction. The three respective temperatures differ. In the convergent part the temperature in the  $y$ -direction,  $T_y$ , is highest, while in the divergent part  $T_y$  is lower than  $T_x$  and  $T_z$ .  $T_z$  is only influenced by collisions between particles because there is no wall in  $z$ -direction. Comparing the two nozzles presented in Fig. 5, we observe the expected trend that the temperature anisotropy decreases with increasing nozzle size. At the end of the nozzles in Fig. 5 the temperature anisotropy grows because the collision rate between particles drops as the density drops. Whether the random particle velocities are Maxwell-Boltzmann distributed will be studied in section IV about microscopic properties.

In table II we compare the difference  $\Delta x_c = x_c - x_c^0$  between the calculated position  $x_c$  of the sonic horizon and the position  $x_c^0$  of minimal cross section area predicted by isentropic flow in the continuum description. In all cases the sonic horizon is “delayed” and shifted downstream,  $\Delta x_c > 0$ . With growing nozzle size characterized by the throat width  $d_m$ , the dimensionless difference falls in relation to the nozzle size, quantified by the ratio  $\frac{\Delta x_c}{d_m}$  shown in the right column. In absolute numbers,  $\Delta x_c$  grows with size (middle column), until it actually drops for the largest nozzle. Surprisingly, our atomistic simulations indicate that for a sufficiently large nozzle the sonic horizon is situated right in the middle, with atomistic precision.

### C. Phase diagram

Does the gas undergo a phase transition and condense into droplets at the end of the nozzle as it cools upon expansion? Fig. 6 shows the phase diagram of the LJ equation of state in the  $(T, \rho)$  plane as determined from Ref. [33]. The saturation density curve shown in yellow is associated with the phase transition, but up to

the critical density, shown as blue curve, a supersaturated vapor phase or a superheated liquid phase is possible. This supersaturated and superheated phases are metastable. The green curve in Fig. 6 shows the path of density and temperature values, shown in panels c) and i) of Fig. 5, of the gas expansion in the nozzle with throat width  $d_m = 31.25$ . Strictly speaking, only an adiabatically slow evolution of a LJ fluid has a well-defined path in diagram Fig. 6, which shows *equilibrium* phases. But plotting the state during expanding through the microscopic nozzle in Fig. 6 at least provides a qualitative description of the fluid at a particular position in the nozzle. The path would extend to about  $T = 0.4$ , but the equation of state from ref. [33] does not reach below  $T = 0.7$ . We note that the triple point, obtained from molecular simulations studies in Ref.[38] lies at  $T_{tr} = 0.661$ , below which the gas-liquid coexistence region becomes a gas-solid coexistence region.

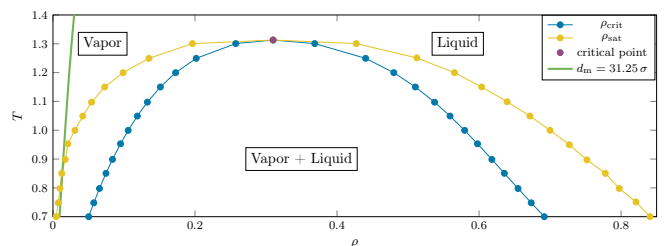


FIG. 6. Density-temperature phase diagram. Shown are the saturation density (yellow), the critical density (blue) and the critical point (purple) from the Lennard-Jones equation of state [33]. For the nozzle with a throat width  $d_m = 31.25$  the path of temperature and density values are shown as green curve.

From the path traced by the expanding gas we see that the LJ fluid starts in the gas phase in the inlet. As temperature and density fall upon expansion, the fluid enters the gas-liquid coexistence region. In this region the fluid can remain in a metastable supersaturated gas phase. Below the triple point, even the gas-solid coexistence region is reached at the end of the nozzle.

Our simulations show no evidence of a liquid or even a solid phase in our simulations, which would appear as small liquid or solid clusters; the LJ particles remain unbound until reaching the outlet region of the nozzle. Either the gas remains metastable or it is too far out of local thermal equilibrium that the discussion in terms of the phase diagram is meaningless. The anisotropy of the temperature discussed in the previous section indicates that thermal equilibrium is not completely fulfilled. The absence of nucleation of clusters is not a surprise, because there is simply not enough time in a microscopic nozzle for nucleation under such dilute conditions before the gas reaches the outlet.



## IV. MICROSCOPIC PROPERTIES

Molecular dynamics simulation allows to measure properties which are inaccessible in a macroscopic continuum mechanical description. We already have seen in the previous section the temperature is slightly anisotropic, which is inconsistent with local equilibrium. In this section we take a closer look at quantities defined on an atomistic level: the velocity probability distribution (in equilibrium the Maxwell-Boltzmann distribution) and the velocity autocorrelation function. Furthermore we study the propagation of density waves by calculating the upstream and downstream time-correlations of thermal density fluctuations of the stationary flow before, at, and after the sonic horizon. The goal is to check if the sonic horizon, found in the previous section by thermodynamic consideration, is also a well-defined boundary for upstream information propagation on the microscopic level.

### A. Velocity Distribution

We have observed a temperature anisotropy, see panel c) and d) in Fig.5. This raises the question whether the particle velocities even follow a Maxwell-Boltzmann distribution. If the velocities are not Maxwell-Boltzmann distributed, we do not have a well-defined kinetic temperature. This question is important for the interpretation of the results, for example when we discussed the temperature drop during expansion in the previous section. We now clarify whether it is meaningful to talk about temperature in microscopic nozzles.

We calculate the velocity distribution for the two largest nozzles (see Fig.5). shown in Fig. 7 by separately sampling the histograms for the  $x$ ,  $y$ , and  $z$ -components of the velocity, where we subtract the steady flow velocity from the particle velocities, see appendix D. Since the velocity distribution depends on the location  $x$  in the nozzle, the histograms are two-dimensional, which requires a lot of data to sample from. Therefore we split  $x$  into only three regions  $x_1$ ,  $x_2$  and  $x_3$ , depicted in the nozzle illustrations at the top of Fig. 7.

The velocity distributions  $f(v_x, x_j)$  for the  $x$ -component of the velocity are shown in panels c) and d) for the two respective nozzles, each panel showing  $f(v_x, x_j)$  for all three regions  $x_j = x_1, x_2, x_3$  in blue, yellow, and green. Of course, the distributions become more narrow for larger  $x_j$ , consistent with a downstream drop of temperature in a Laval nozzle. We fit the histograms with Gaussian functions, i.e. the Maxwell-Boltzmann distribution, also shown in the panels. The corresponding results  $f(v_y, x_j)$  and  $f(v_z, x_j)$  for the other two velocity directions are shown in panels e)–h). It is evident that, apart from small statistical fluctuations, the Maxwell-Boltzmann distribution is a good fit in all cases. Thus the notion of temperature in these microscopic non-equilibrium systems makes sense.

The width of the velocity distributions (i.e. the temperature) is not quite the same in the three directions, however, in particular in region  $x_3$ , the diverging part of the nozzle. In order to see this better, we compare the fits to  $f(v_i, x_3)$  for  $i = x, y, z$  in panels i) and j). The distribution of the  $y$ -component of the velocity is narrower than the other two directions. In other words the temperature according to  $v_y$  is lower, thus the temperature is not isotropic. This means there is insufficient equilibration between the three translational degrees of freedoms. The effect is more pronounced for the smaller nozzle because particles undergo fewer collisions before they exit the nozzle, as quantified by the larger Knudsen number, see Fig.5.

The spatial binning into just three region  $x_j$  is rather coarse-grained as it neglects the temperature variation within a region. With more simulation data a finer spatial resolution would be possible, however we feel that the presented results are convincing enough that the thermal kinetic energy can be well-characterized by a temperature, albeit slightly different in each direction.

### B. Velocity Autocorrelation Function

The velocity auto-correlation function, VACF, quantifies the “memory” of particles about their velocity. The VACF is defined as

$$\text{VACF}(\tau) = \langle \mathbf{v}_p(t) \cdot \mathbf{v}_p(t + \tau) \rangle_{t,p} \quad (10)$$

with  $\mathbf{v}_p(t)$  the velocity of particle  $p$  at time  $t$ .  $\langle \dots \rangle_{t,p}$  denotes an average over time and over all particles. An ideal, i.e. non-interacting particle has eternal memory,  $\text{VACF}_u(\tau) = \text{const}$ . But due to interactions with the other particles,  $\text{VACF}_u(\tau) \rightarrow 0$  within microscopically short times.

In the case of stationary flow, we need to subtract the flow velocity from particle velocities in eq (10). Furthermore, the VACF will depend on the  $x$ -coordinate in the nozzle. Therefore we generalize eq. (10) to a form which is suitable for stationary flow in a nozzle that depends on  $x$  and is not biased by the flow velocity. We also normalize the VACF such that it is unity at  $\tau = 0$ :

$$\text{VACF}(x, \tau) = \frac{\langle \Delta \mathbf{v}_p(t) \cdot \Delta \mathbf{v}_p(t + \tau) \delta(x - x_p(t)) \rangle_{t,p}}{\langle \Delta \mathbf{v}_p(t)^2 \delta(x - x_p(t)) \rangle} \quad (11)$$

where  $\Delta \mathbf{v}_p(t) \equiv \mathbf{v}_p(t) - \mathbf{v}(x_p(t))$  is the thermal part of the velocity, after subtraction of the flow velocity  $\mathbf{v}$  at the particle coordinate  $x_p(t)$ . Note that we define  $\text{VACF}(x, \tau)$  such that the spatial coordinate  $x$  coincides with the starting point  $x_p(t)$  at time  $t$  of the time correlation; at the final time  $t + \tau$ , the particle has moved to  $x_p(t + \tau)$  downstream. When we sample (11) with a MD simulation, the coordinate  $x$  and the correlation time  $\tau$  are discretized, and  $\delta(x - x_p(t))$  is replaced by binning a histogram in the usual fashion, see the appendix.

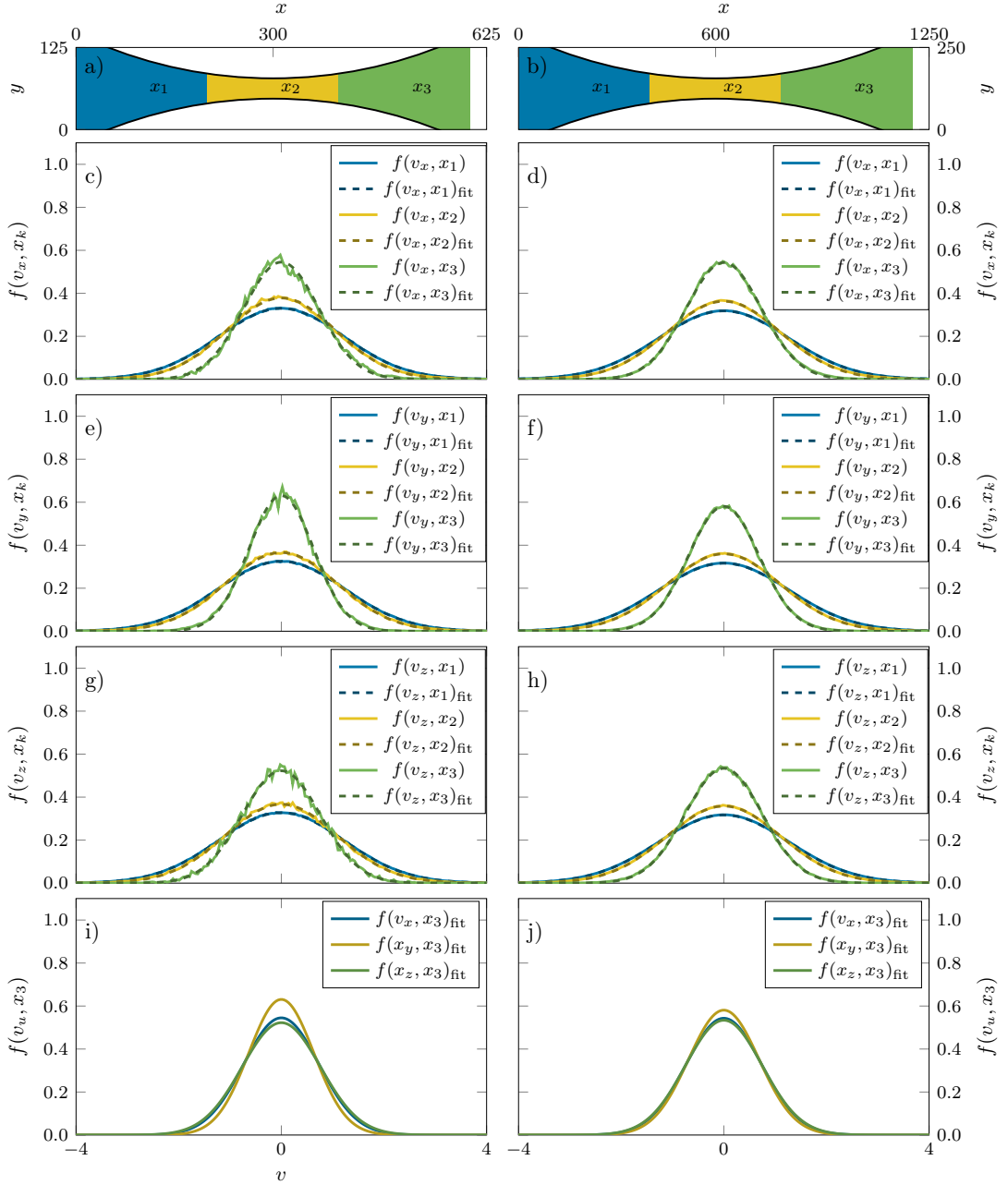


FIG. 7. Thermal part of the particle velocity distribution  $f(v_i, x_j)$  for two nozzle sizes with a throat width of  $31.25\sigma$  and  $62.5\sigma$  in the left and right column, respectively. Panels a) and b) show a schematic representation of those nozzles with the three regions  $x_1$ ,  $x_2$ , and  $x_3$  for which the velocity distributions are obtained from the MD simulations. Panels c) to h) show the velocity distribution of the components  $v_x$ ,  $v_y$  and  $v_z$  for the different regions in the nozzle. Also shown are Gaussian fits (dashed lines). Panel i) and j) are comparing the fits to the three velocity components these fits in the  $x_3$  region, in the diverging part of the nozzle.

Fig. 8 shows the VACF for various positions  $x$  in the nozzle. The calculations were done for two different nozzle sizes (left and right panels). The VACFs cannot be shown for  $x$  all the way to the end of the nozzles because particles leave the simulation before the velocity correlation can be evaluated. For example, if a particle in the smaller of the two nozzles in Fig. 8 is located at  $x = 437$

at  $\tau = 0$  it will have moved with the flow on average to  $x = 537$  at  $\tau = 50$ , where the outlet region starts and particles are removed from the simulation. For  $x$  close to the outlet, the VACF would be biased because the average in eq. (11) would contain only particles which happen to travel slow, e.g. slower than the flow average.

The VACF decays monotonously for all  $x$  (in fact,

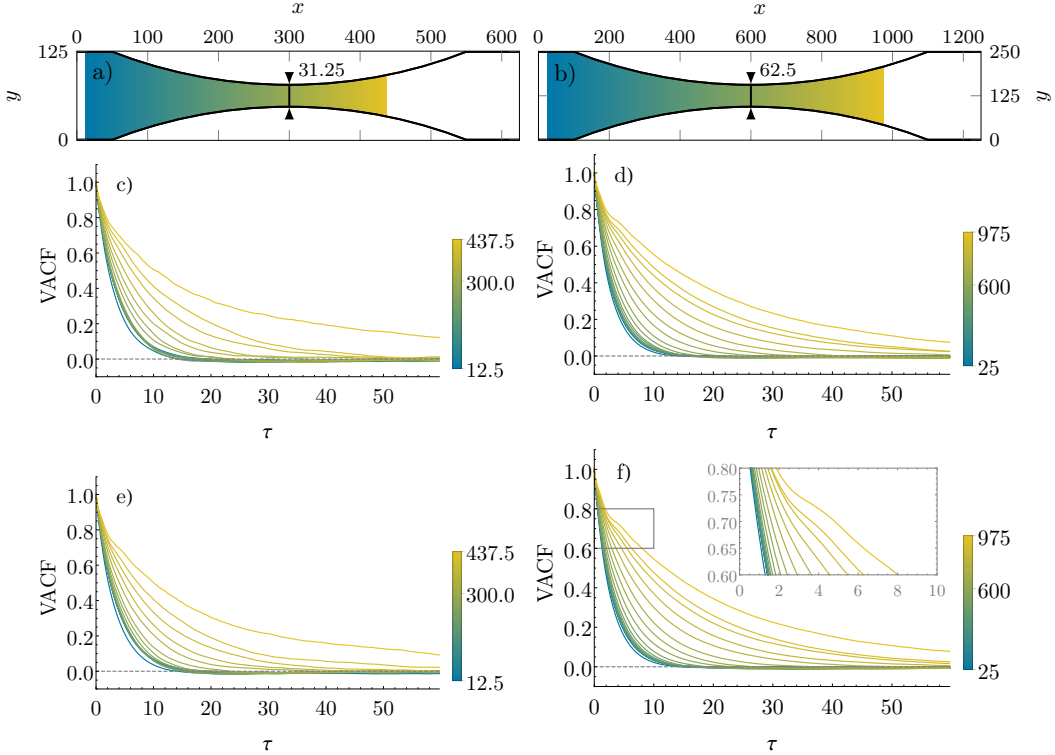


FIG. 8. Normalized velocity auto-correlation function  $VACF(x, \tau)$ , eq. (11), along the nozzle with color coded  $x$ -position. Panels a) and b) show the shape and size of two nozzles, indicating the color scale for  $x$  in the panels below. Panels c) and d) show the VACF for nozzles with a distance  $z_{max} = 43.1\sigma$  between the periodic boundaries in  $z$ -direction. Panels e) and f) show the same for  $z_{max} = 86.2\sigma$ . The inset of panel f) shows a close-up of the shoulder around  $\tau = 4$ , discussed in the text.

the VACF for only the  $y$ -component of the velocity (not shown) slightly overshoots to a negative correlations in the divergent part of the nozzle, which is a trivial effect of wall collisions). The decay is slower further downstream because the density drops. Towards the ends of the nozzles, the mean free path becomes large, see Fig. 5, reaching the length  $z_{max}$  of the simulation box in  $z$ -direction, where periodic boundary conditions are applied. We demonstrate that the finite size bias in  $z$ -direction is negligible by comparing the VACFs for different choices of  $z_{max}$ . If  $z_{max}$  were too small, two particles might scatter at each other more than once due to the periodic boundaries, which would lead to a spurious oscillation in the VACF. Panels e) and f) in fig. 8 show  $VACF(x, \tau)$  for  $z_{max} = 86.2\sigma$ , twice as large as in panels c) and d), corresponding to twice as many particles. Apart from the smaller statistical noise for larger  $z_{max}$ , the VACFs for  $z_{max} = 43.1\sigma$  and  $z_{max} = 86.2\sigma$  are identical. This confirms that  $z_{max} = 43.1\sigma$  is large enough to obtain reliable results.

An interesting feature in the VACF for both nozzle sizes shown in Fig. 8 is a small shoulder around  $\tau \approx 4$  in the divergent part, i.e. a small additional velocity correlation. The inset in panel f) of Fig. 8 shows a close-up of the shoulder. Since this happens only at the low density in the divergent part of the nozzle, where

the three-body collisions rate is low, the shoulder can be expected to be a two-body effect. It is consistent with pairs of particles orbiting around each other a few times. We test this conjecture by estimating the orbit period of two bound atoms in thermal equilibrium. The orbit speed  $v$  shall be determined by the temperature  $T$ . We further assume a circular stable orbit with diameter  $d$ . The orbiting particles have two rotational degrees of freedom but also two times the mass of a single particle:

$$\frac{1}{2}k_B T = \frac{1}{2}mv^2. \quad (12)$$

The centrifugal force  $F_c$  and the attractive LJ force  $F_{LJ}$  must be balanced,

$$F_c + F_{LJ} = m \frac{2v^2}{d} - 4\epsilon m \left( -\frac{12}{d^{13}} + \frac{6}{d^7} \right) = 0, \quad (13)$$

The orbit period  $t_{rot}$  can now be calculated from eq. (12) and eq. (13)

$$t_{rot} = \pi \frac{d}{v} = \pi \left( \frac{6\epsilon m^4 \pm \sqrt{36\epsilon^2 - 24k_B T/m}}{k_B^4 T^4} \right)^{1/6}. \quad (14)$$

which expresses  $t_{rot}$  as function of the temperature. When we plug in a typical temperature towards the end

of the nozzles of  $T \approx 0.5$ , we obtain an orbit time  $t_{\text{rot}} \approx 5$ , which is similar to the time when the shoulder in the VACF appears, see Fig. 8. This does not mean that bound dimers form in the supercooled flow near the exit of the nozzle, which requires three-body collisions. But the estimate based on bound states is applicable also to spiral-shaped scattering processes where two particles orbit each other. The good agreement between the  $t_{\text{rot}}$  and the shoulder indicates that such scattering processes occur, and may be a seeding event for the nucleation of van der Waals clusters and condensation in larger nozzles.

### C. Density fluctuation correlations and the sonic horizon

The calculation of the speed of sound  $c$  according to eq.(2), using the equation of state from Ref.[33], assumes local thermal equilibrium. However, the anisotropy of the temperature, see Fig. 5, shows that not all degrees of freedom are in local equilibrium during the fast expansion through a microscopic nozzle. Therefore, locating the sonic horizon may be biased by non-equilibrium effects. It's not even clear if a sonic horizon, the definition of which is based on macroscopic fluid dynamics, is microscopically well-defined. While the thermal velocities of the atoms follow Maxwell-Boltzmann distributions, there are always particles in the tails of the distribution that travel upstream even after the sonic horizon. So maybe information can travel upstream on the microscopic scale of our nozzles, negating the existence of a sonic horizon.

The MD methods provides the microscopic tools to answer this question by calculating spacetime correlations of density fluctuations: if density fluctuations propagate upstream even in the divergent part of the nozzle, there is no sonic horizon. We quantify the density fluctuation correlations before, at, and after the sonic horizon predicted from the calculation of the speed of sound. The instantaneous density  $\rho(x, t)$  at position  $x$  and time  $t$  is evaluated according to eq. (A2). The density fluctuation, i.e. the random deviation at time  $t$  from the average density at position  $x$ , is obtained by subtracting the time-averaged density (shown in Figs. 3, 4, and 5) from  $\rho(x, t)$ ,  $\Delta\rho(x, t) = \rho(x, t) - \langle \rho(x, t) \rangle_t$ . Note that fluctuations of the density depend also on  $y$  and  $z$ , but we are interested in the fluctuations relative the the sonic horizon, and thus fluctuations between different positions  $x$  in the nozzle. The correlation between a density fluctuation at  $x$  and  $t$  and a density fluctuation at  $x + \delta x$  and  $t + \tau$  is given by the time average

$$S(\tau, x, \delta x) = \frac{\langle \Delta\rho(x, t) \Delta\rho(x + \delta x, t + \tau) \rangle_t}{\langle \Delta\rho(x, t) \Delta\rho(x, t) \rangle_t} \quad (15)$$

$S$  is normalized such that it is unity for zero spatial and temporal shifts,  $S(0, x, 0) = 1$ .

In Fig. 9 we show the density fluctuation correlations  $S(\tau, x, \delta x)$  in a nozzle with throat width  $31.25\sigma$ , evaluated at 6 different positions  $x$  in the nozzle and for three

relative position offsets  $\delta x = p\sigma$  with  $p \in \{-1, 0, 1\}$ . The position  $x$  in the nozzle is indicated in an inset in each panel. The density binning, with bin size  $\sigma$ , is illustrated at the top of Fig. 9, which shows three adjacent bins at  $x$ ,  $x + \sigma$  and  $x - \sigma$ , corresponding to  $p/\sigma = -1, 0, 1$  in the figure labels.

The self correlation  $S(\tau, x, 0)$  (yellow curves), correlating only the temporal decay of the density correlations at  $x$ , is mainly influenced by the flow velocity and decays faster for higher flow velocities because density fluctuation are transported away more quickly.

The upstream correlations  $S(\tau, x, -\sigma)$  (blue curves) and the downstream correlations  $S(\tau, x, \sigma)$  (green curves) are more interesting. Both correlations are small at zero delay time  $\tau = 0$ , because a density fluctuation at  $x$  needs some time to disperse to neighboring density bins. At position  $x = 10$ , where the flow speed is still small, there is no noticeable difference between upstream and downstream correlation. For larger  $x$ , hence for larger flow speed, the forward correlation increases and the backward correlation decreases, because the density fluctuation disperses with the flow or against the flow, respectively.

According to the local speed of sound calculated in the previous section, see table II, there is a sonic horizon at  $x = 306$  for the nozzle size in Fig. 9. Indeed, for  $x = 300$ , the backward correlation has no peak anymore, but decreases monotonously from a small non-zero value at  $\tau = 0$ . For even larger  $x$ , the upstream correlation decays more rapidly, yet it never completely vanishes at  $t = 0$ . The reason for this apparent contradiction to the existence of a sonic horizon is that the distance between bins and the width of the bins are both  $\sigma$ . The finite value at  $\tau = 0$  is an artifact caused by the density bins being directly adjacent to each other, see the illustration in Fig. 9: a density fluctuation at  $x$  will immediately have an effect on the adjacent bins at  $x + \sigma$  and  $x - \sigma$  since they share a boundary.

In order to remove this bias, we also calculated the correlations with offsets  $\delta x = \pm 2\sigma$ ,  $S(\tau, x, 2\sigma)$  and  $S(\tau, x, -2\sigma)$ , such that the upstream and downstream bins do not share a boundary with the bin at  $x$ . In Fig. 10 we compare the two choices of offsets. The left panels are take from Fig. 9 where  $\delta x \in \{-\sigma, 0, \sigma\}$ ; the right panels show  $S(\tau, x, \delta x)$  with  $\delta x \in \{-2\sigma, 0, 2\sigma\}$ , with a twice as large  $\tau$  range, because density fluctuations have to travel twice as far. The upstream and downstream correlations now vanish for zero time delay  $\tau = 0$ . The upstream correlation  $S(\tau, x, -2\sigma)$  right at the throat at  $x = 300\sigma$  is very small but does not quite vanish, which is consistent with a location of the sonic horizon predicted at  $x = 306\sigma$  according to the speed of sound. Further downstream at  $x = 350\sigma$ , however,  $S(\tau, x, -2\sigma)$  indeed vanishes within the error bars. This means that information about density fluctuations cannot travel backwards beyond the sonic horizon even on the microscopic scale of just a distance of  $2\sigma$ . A microscopic Laval nozzle does have a sonic horizon.

We also calculated the density fluctuation correlations

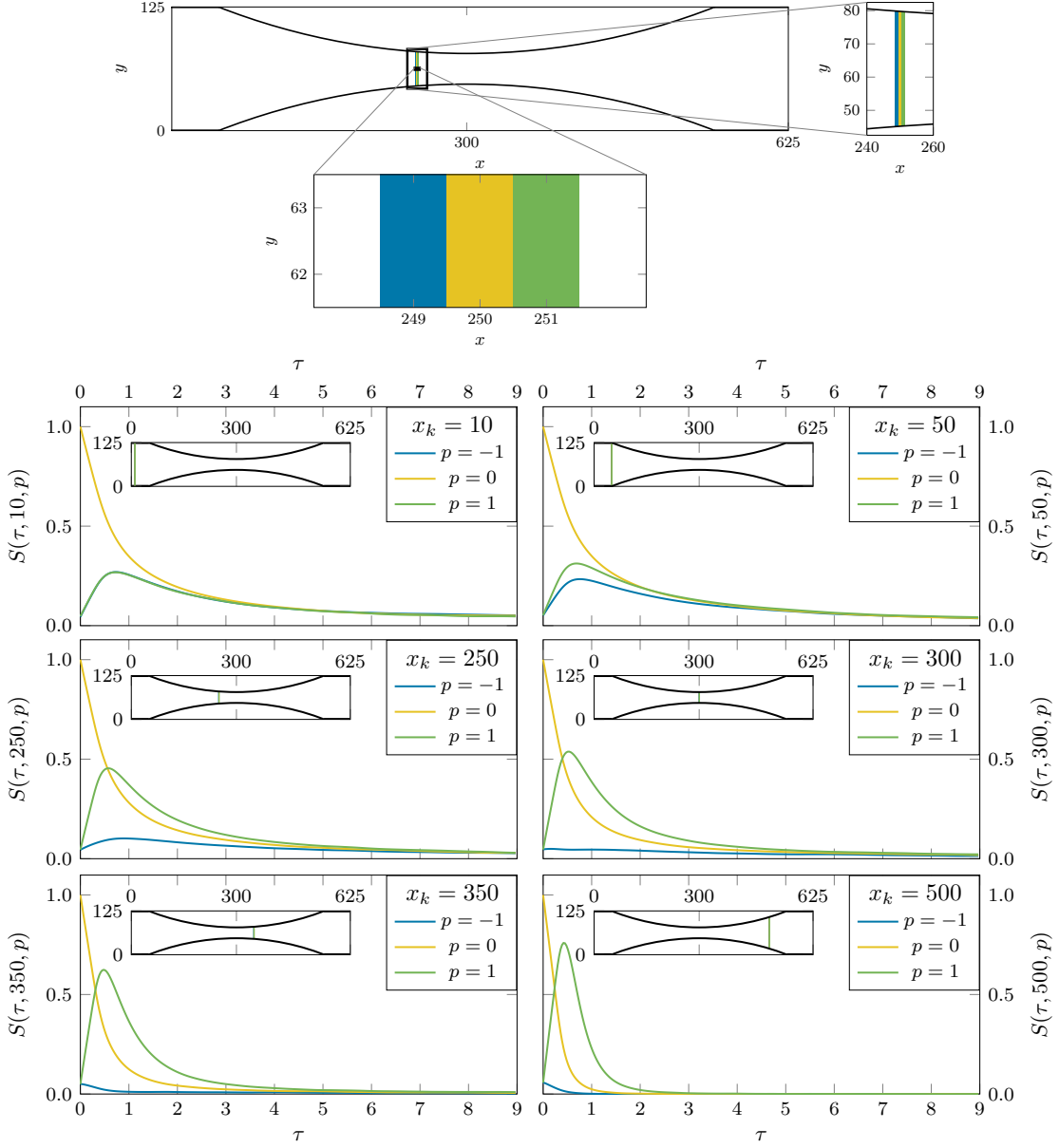


FIG. 9. Density fluctuation correlations  $S(\tau, x, \delta x)$ , eq. (15). Panels a) to f) show the self correlation  $S(\tau, x, 0)$  in yellow, a backward correlation  $S(\tau, x, -\sigma)$  in blue and a forward correlation  $S(\tau, x, \sigma)$  in green for different positions  $x$  in the nozzle as given in the insets. The illustration at the top shows the density bins used for calculating  $S(\tau, x, \delta x)$ :  $S(\tau, x, 0)$  is obtained by correlating the yellow bin with itself,  $S(\tau, x, \sigma)$  or  $S(\tau, x, -\sigma)$  are obtained by correlating the yellow bin with the green or blue bin, respectively.

for a nozzle twice as large (length  $L = 1250\sigma$  and throat width  $d = 62.5\sigma$ ). Fig. 11 compares the corresponding results with those shown in Fig. 10. For the comparison, we scaled all lengths by two: the bins are  $2\sigma$  wide, separated by  $4\sigma$ , see illustration at the top of Fig. 11. We compare  $S(\tau, x, \delta x)$  of the smaller nozzle with  $S(2\tau, 2x, 2\delta x)$  of the larger one, i.e. at the same relative positions with the same relative upstream and downstream offset, and showing twice the time window for the larger nozzle. According to the speed of sound, the sonic horizon for the

larger nozzle is located at  $x = 603\sigma$  (see table II), very close to the throat at  $x = 600\sigma$ . The comparison in Fig. 11 shows that the density fluctuation correlations are very similar for equal relative positions for both nozzles. Also for the larger nozzle, the correlations are very small at the throat. Further downstream at  $x = 350\sigma$  and  $x = 700\sigma$ , respectively, both nozzles exhibit no upstream correlations.

Our calculations confirm that the thermodynamic determination of a sonic horizon, based on the equation of

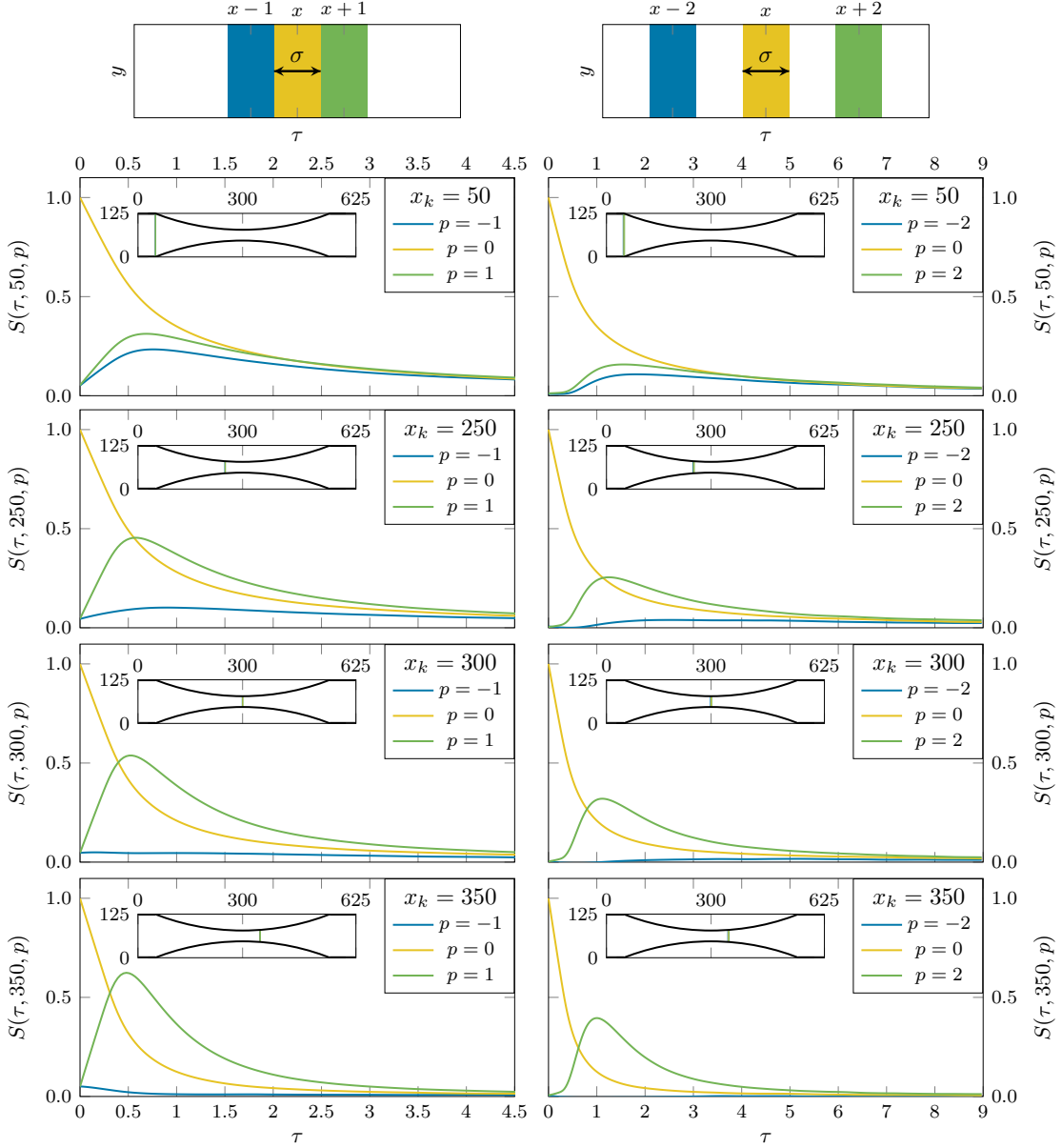


FIG. 10. Comparison of density fluctuation correlation  $S(\tau, x, p\sigma)$  for different offsets,  $p \in \{-1, 0, 1\}$  (left panels) and  $p \in \{-2, 0, 2\}$  (right panels). At the top the respective binning is illustrated. In the insets the reference position  $x$  is indicated. The sonic horizon is situated slightly downstream of the nozzle throat ( $x = 300$ ) at  $x = 306$ , according to the thermodynamic calculation of the local speed of sound.

state, is valid, although the anisotropy of the temperature indicates that the rapid expansion through the nozzles hinder complete local thermal equilibrium. The location of the sonic horizon is consistent with the vanishing of upstream time correlations of density fluctuations. The existence of a microscopically narrow sonic horizon is a non-trivial result, considering the large estimated Knudsen numbers.

## V. CONCLUSION

We studied the expansion of a gas of Lennard-Jones particles and its transition from subsonic to supersonic flow through microscopic Laval slit nozzles into vacuum. Our goal was to assess to what extent Laval nozzles with throat widths down to the scale of a few atom diameters still follow the same mechanisms as macroscopic nozzles where, given a sufficiently low outlet pressure, the gas flow becomes supersonic in the nozzle throat. For our study we used non-equilibrium molecular dynamics

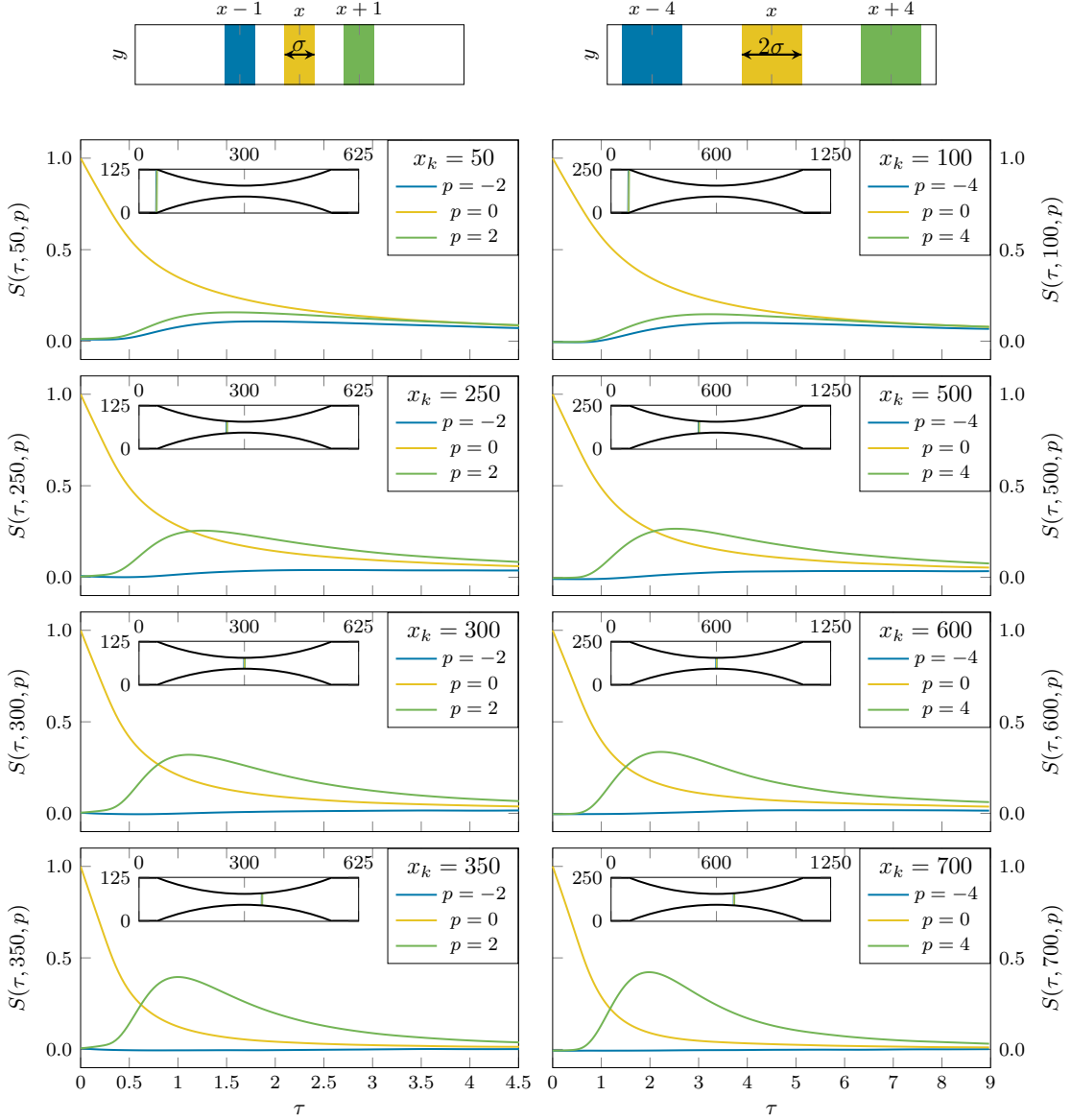


FIG. 11. Comparison of the density fluctuation correlations  $S(\tau, x, \delta x)$  for two nozzle with throat width  $d = 31.25 \sigma$  (left panels) and  $d = 62.5 \sigma$  (right panels), respectively. All lengths are scaled by two for the larger nozzle, such that we compare the correlations for equal relative positions. At the top the density bin spacing is illustrated and the insets show the positions  $x$ .

(MD) simulations. MD is computationally demanding but makes the fewest approximations. We considered idealized nozzles with atomically flat surfaces with perfect slip to avoid boundary layer effects.

We introduced three thermodynamic regions for the non-equilibrium molecular dynamic simulation: an inlet region, the nozzle region and the outlet region. In the inlet and outlet region, particle insertions and deletions are realized by grand canonical Monte Carlo sampling [29]. After equilibration this allows to study stationary flows.

We obtained the thermodynamic state variables temperature, density, flow velocity, and pressure and their

spatial dependence, as well as the Knudsen number, Mach number, velocity auto-correlation, and velocity distribution of the gas for nozzles of different sizes. We found a well-defined sonic horizon, i.e. the surface where the flow becomes supersonic, and analyzed it via space-time correlations of density fluctuations. We studied how the expansion dynamics depend on the nozzle size. Lower temperatures and correspondingly higher velocities and Mach numbers of the expanding gas are reached for larger nozzles, converging to predictions for isentropic expansion of an ideal gas continuum.

With non-equilibrium molecular dynamics we can ob-

serve phenomena which cannot be studied in continuum fluid dynamics, which assumes local thermodynamic equilibrium. We found that this assumption is violated for microscopic nozzles. The kinetic energy in the three translational degrees of freedom cannot equilibrate completely and is slightly different for each individual translational degree of freedom. The velocity components are still Maxwell-Boltzmann distributed, with a different width for each direction, which corresponds to an anisotropic temperature.

The phase of the LJ fluid in the inlet is in a vapor phase, but upon expansion through the nozzle becomes supersaturated. At the end of the nozzle it is in the vapor-solid coexistence phase. Indeed, in the velocity auto-correlation function, VACF, we see indications of metastable pairs of particles. Since the expanding gas does not reach equilibrium in our microscopic nozzles, no clusters are formed. Cluster formation could be studied by enlarging the simulation and including the low density region after the nozzle, giving the fluid enough time to equilibrate.

The investigation of the sonic horizon with the help of spacetime-dependent correlations of density fluctuations showed that the position of the sonic horizon obtained from calculating the local speed of sound matches the position where density correlations practically cannot propagate against the flow. A microscopic distance on the order to the LJ particle size  $\sigma$  is already enough to completely suppress the backward correlations. The vanishing of backward time correlations does of course not happen abruptly at the sonic horizon, instead the backward correlations decrease gradually with the increasing flow velocity toward the sonic horizon. At the same time the forward correlations increase with the flow velocity. For larger microscopic nozzles, the simple macroscopic description relating the cross section to the Mach number is quite accurate. For smaller nozzles the position of the sonic horizon is shifted downstream.

In future work, it will be interesting to study nozzles with rough walls. The gas expansion through microscopic nozzle will be strongly affected by the boundary layer near the walls. Another topic of practical interest is the co-expansion of a carrier noble gas seeded with molecules to investigate the cooling efficiency of rotational and vibrational degrees of freedom of the molecules. This models the cooling of molecules for molecular beam spectroscopy. We note that nozzles for molecular beam spectroscopy are significantly larger than those studied here, with nozzle diameters of the order of tens of  $\mu m$ , instead of tenths of  $nm$ . Increasing the outlet region will allow to study not only the condensation of the gas into clusters, but also the effect of a finite exit pressure on the position of the sonic horizon [13].

We acknowledge inspiring discussions with Stefan Pirker.

## Appendix A: Density calculation

The density  $\rho(x)$  as function of position  $x$  in the nozzle is calculated by binning the  $x$ -coordinate of all particles. Since we are interested in stationary flow situations, we can take time averages of the number of particles in the bin of volume  $V_{\text{bin}}(x)$ . The binning volumes are slices, usually of thickness  $\sigma$ , which are centered at  $x$ , as illustrated in Fig. 12. This average can be written as

$$\rho(x) = \left\langle \frac{1}{V_{\text{bin}}(x)} \sum_{i:p_i \in V_{\text{bin}}(x)} 1 \right\rangle_t \equiv \langle 1 \rangle_{t, V_{\text{bin}}(x)} \quad (\text{A1})$$

with the sum counting all particles  $p_i$  in the volume of bin  $V_{\text{bin}}(x)$ , and the bracket denoting the time average. For calculations of spacetime density correlations we need the instantaneous density at  $x$  at time  $t$ , which we obtain by omitting the time average in eq. (A1)

$$\rho(x, t) = \frac{1}{V_{\text{bin}}(x)} \sum_{i:p_i \in V_{\text{bin}}(x)} 1 \quad (\text{A2})$$

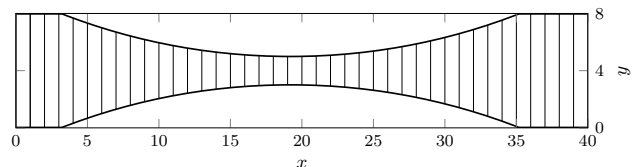


FIG. 12. Bin volumes of width  $\sigma$  used for calculating the density  $\rho(x)$ .

The determination of  $V_{\text{bin}}(x)$  is not trivial, since the wall is not a well-defined hard boundary, but realized by the LJ potential (4). Choosing  $z = 0$  in eq. (4) for the volume calculation would overestimate the real volume effectively available for the particles, because it neglects the thickness of the “skin” due to the finite value of  $\sigma$ . We determined that  $z = 0.8\sigma$  is the most suitable choice in the following way: we simulated a small nozzle (the size depicted in Fig. 12) with a constriction so narrow that almost no particle pass through in the course of a simulation. The wall position  $z$ , and hence the effective volume  $V_{\text{bin}}(x)$ , is determined such that the density  $\rho(x)$  in the left half of the nozzle, obtained from (A1), is constant as expected for an equilibrium simulation in a closed geometry. If the skin thickness were over- or underestimated, we would obtain a density increase or decrease towards the constriction, respectively.

## Appendix B: Pressure calculation

The pressure is calculated from the diagonal elements of the stress tensor which is calculated for each individual



particle  $i$  as [30, 36]

$$S_{iab} = -m_i v_{ia} v_{ib} - \frac{1}{2} \sum_{\substack{j: p_j \in V_i \\ j \neq i}} (r_{ia} F_{ijb} - r_{ja} F_{ijb}) \quad (\text{B1})$$

with  $a, b \in \{x, y, z\}$  the Cartesian components. The first term is the ideal gas contribution and is biased by the collective flow speed. Since only the thermal motion should contribute to  $S_{iab}$ , the flow velocity must be subtracted from  $\vec{v}_i$ , see section C below for the calculation of the flow velocity. The second term is the virial contribution from the LJ-interaction. The summation is over all particles  $j$  within  $r_c$  from particle  $i$ , where  $r_c$  is the cut-off radius of the LJ potential. This defines the cut-off volume  $V_i$  of particle  $i$ .  $r_{ia}$  is component  $a \in \{x, y, z\}$  of the coordinate of particle  $i$  and  $F_{ijb}$  the component  $b$  of the force of the pairwise interaction between particle  $i$  and  $j$ . We calculate the pressure  $p(x)$  at position  $x$  in the nozzle by averaging the diagonal elements of the stress tensor  $S_{iab}$  over all particles  $i$  within the bin volume  $V_{\text{bin}}(x)$ ,

$$p(x) = - \left\langle \frac{\rho(x)}{3} (S_{iix} + S_{iyy} + S_{izz}) \right\rangle_{t, V_{\text{bin}}(x)} \quad (\text{B2})$$

with  $\langle \rangle_{V_{\text{bin}}(x)}$  denoting the average over  $V_{\text{bin}}(x)$ . We also average over the three diagonal elements because we assume an isotropic stress tensor. Remembering that the temperature is not isotropic in the nozzle, the assumption of an isotropic stress tensor may not be valid. Inserting the stress tensor (B1) into the expression (B2) for the local pressure, we obtain

$$p(x) = \rho(x) k_B T(x) + \frac{1}{3} \left\langle \sum_{\substack{j: p_j \in (V_i \cap V_{\text{bin}}(x)) \\ j \neq i}} \mathbf{r}_i \mathbf{F}_{ij} \right\rangle_{t, V_{\text{bin}}(x)} + \frac{1}{6} \left\langle \sum_{\substack{j: p_j \in (V_i \setminus V_{\text{bin}}(x)) \\ j \neq i}} \mathbf{r}_j \mathbf{F}_{ji} \right\rangle_{t, V_{\text{bin}}(x)} \quad (\text{B3})$$

where in the calculation of the local virial we have to distinguish between neighbor particles  $p_j$  which are also in the same binning volume  $V_{\text{bin}}(x)$  as particle  $p_i$  (giving rise to the first virial expression with the common prefactor  $\frac{1}{3}$ ) and those which are not (the second virial expression with the prefactor  $\frac{1}{6}$ ). For the first virial expression we could use  $\mathbf{F}_{ij} = -\mathbf{F}_{ji}$  and swap the summation index  $i$  and  $j$  leading to a factor 2. For the particles  $p_j$  which are not in volume  $V_{\text{bin}}(x)$  this cannot be done, and each force  $\mathbf{F}_{ij}$  contributes just once.

### Appendix C: Calculation of Velocity

The velocity field  $\mathbf{v}(x, y)$  in the nozzle depends on both the  $x$  and  $y$ -coordinate. The velocity is not only a key quantity for Laval nozzles, but also required for obtaining the temperature  $T$ , because  $\mathbf{v}(x, y)$  needs to be subtracted from the particle velocities for the calculation of

$T$ , see next section. Fig. 13 illustrates the bin volumes  $V_{\text{bin}}(x, y)$  for the calculation of  $\mathbf{v}(x, y)$ , as opposed to the bin slices in Fig. 12. The time averaged flow velocity  $\mathbf{v}$

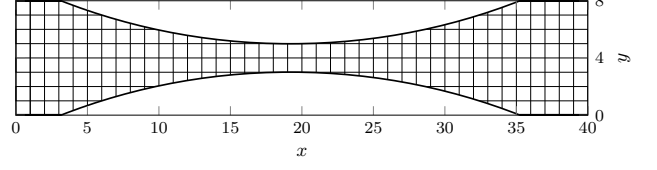


FIG. 13. Bin volumes  $V_{\text{bin}}(x, y)$  with side length  $\sigma$  in  $x$ - and  $y$ -direction.

in a bin volume  $V_{\text{bin}}(x, y)$  can be calculated as

$$v_a(x, y) = \left\langle \frac{1}{N(x, y)} \sum_{i: p_i \in V_{\text{bin}}(x, y)} v_{ai} \right\rangle_t \quad (\text{C1})$$

with  $a \in \{x, y, z\}$ ,  $v_{ai}$  is the velocity component  $a$  of particle  $p_i$ , and  $N(x, y)$  the number of particles in  $V_{\text{bin}}(x, y)$  at a given time. The magnitude of the flow velocity is

$$v(x) = \sqrt{\langle v_x(x, y) \rangle_y^2 + \langle v_y(x, y) \rangle_y^2} \quad (\text{C2})$$

On average there is no flow in  $z$ -direction,  $v_z(x, y) = 0$ .

### Appendix D: Temperature calculation

In order to investigate how the gas cools upon expanding supersonically through the nozzle, we need to calculate the position-dependent temperature  $T(x)$ . The microscopic definition of the temperature is the kinetic energy of the *random* part of the particle velocity, hence we need to subtract the flow velocity  $\mathbf{v}(x, y)$  discussed in the previous section:

$$k_B T(x, y) = m \left\langle \frac{1}{3N(x, y) - 3} \sum_{i: p_i \in V_{\text{bin}}(x, y)} (\mathbf{v}_i - \mathbf{v}(x, y))^2 \right\rangle_t \quad (\text{D1})$$

We are interested only in the  $x$ -dependence of the temperature and therefore we average over  $y$

$$T(x) = \langle T(x, y) \rangle_y \quad (\text{D2})$$

Note that subtracting the flow velocity removes three translational degrees of freedom, which we account for by subtracting 3 from the number of degrees of freedom of the  $N(x, y)$  particles in binning volume  $V_{\text{bin}}(x, y)$ .

In Eq. (D1) we average over the contribution of the three velocity components, which is fine in an isotropic system. In order to test whether the temperature is isotropic or not (and indeed we find it is not), we calculate the direction-dependent kinetic temperature

$$k_B T_a(x, y) = m \left\langle \frac{1}{N(x, y) - 1} \sum_{i: p_i \in V_{\text{bin}}(x, y)} (v_{ia} - v_a(x, y))^2 \right\rangle_t \quad (\text{D3})$$

with  $a \in \{x, y, z\}$ . Again, we are interested only in how

$T_a$  varies with position  $x$  along the nozzle, hence we average over  $y$ ,  $T_a(x) = \langle T_a(x, y) \rangle_y$ .

- 
- [1] William George Unruh, “Experimental black-hole evaporation?” *Phys. Rev. Lett.* **46**, 1351 (1981).
- [2] Matt Visser, “Acoustic black holes: horizons, ergospheres and hawking radiation,” *Class. Quantum Grav.* **15**, 1767 (1998).
- [3] Arthur Kantrowitz and Jerry Grey, “A high intensity source for the molecular beam. part i. theoretical,” *Review of Scientific Instruments* **22**, 328–332 (1951).
- [4] Pamela SH Fitch, Christopher A Haynam, and Donald H Levy, “The fluorescence excitation spectrum of free base phthalocyanine cooled in a supersonic free jet,” *The Journal of Chemical Physics* **73**, 1064–1072 (1980).
- [5] Richard E Smalley, Lennard Wharton, and Donald H Levy, *Molecular optical spectroscopy with supersonic beams and jets*, Tech. Rep. (CHICAGO UNIV ILL DEPT OF CHEMISTRY, 1977).
- [6] TE Gough, RE Miller, and G Scoles, “Infrared laser spectroscopy of molecular beams,” *Applied Physics Letters* **30**, 338–340 (1977).
- [7] Anne R Skinner and Dean W Chandler, “Spectroscopy with supersonic jets,” *American Journal of Physics* **48**, 8–13 (1980).
- [8] Murray V Johnston, “Supersonic jet expansions in analytical spectroscopy,” *Trends in Analytical Chemistry* **3**, 58–61 (1984).
- [9] J Peter Toennies and Andrey F Vilesov, “Superfluid helium droplets: a uniquely cold nanomatrix for molecules and molecular complexes,” *Ang. Chem. Int. Ed.* **43**, 2622–2648 (2004).
- [10] Giovanni Sanna and Giuseppe Tomassetti, *Introduction to molecular beams gas dynamics*, Vol. 226 (World Scientific, 2005).
- [11] Iain D Boyd, Paul F Penko, Dana L Meissner, and Kenneth J Dewitt, “Experimental and numerical investigations of low-density nozzle and plume flows of nitrogen,” *AIAA journal* **30**, 2453–2461 (1992).
- [12] Hideyuki Horisawa, Fujimi Sawada, Kosuke Onodera, and Ikkoh Funaki, “Numerical simulation of micro-nozzle and micro-nozzle-array flowfield characteristics,” *Vacuum* **83**, 52 – 56 (2008).
- [13] Seyed Ali Saadati and Ehsan Roohi, “Detailed investigation of flow and thermal field in micro/nano nozzles using simplified bernoulli trial (sbt) collision scheme in dsmc,” *Aerospace Science and Technology* **46**, 236–255 (2015).
- [14] Ehsan Roohi and Stefan Stefanov, “Collision partner selection schemes in dsmc: From micro/nano flows to hypersonic flows,” *Phys. Rep.* **656**, 1–38 (2016).
- [15] D. C. Rapaport, “Microscale hydrodynamics: Discrete-particle simulation of evolving flow patterns,” *Phys. Rev. A* **36**, 3288 (1987).
- [16] M. Moseler and U. Landman, “Formation, stability, and breakup of nanojets,” *Science* **289**, 1165 (2000).
- [17] K. Kadau, T. C. Germann, N. G. Hadjiconstantinou, P. S. Lomdahl, G. Dimonte, B. L. Holian, and B. J. Alder, “Nanohydrodynamics simulations: An atomistic view of the rayleigh–taylor instability,” *PNAS* **101**, 5851 (2004).
- [18] J. Horbach and S. Succi, “Lattice Boltzmann versus molecular dynamics simulation of nanoscale hydrodynamic flows,” *Phys. Rev. Lett.* **96**, 224503 (2006).
- [19] S. Yasuda and R. Yamamoto, “Synchronized molecular-dynamics simulation via macroscopic heat and momentum transfer: An application to polymer lubrication,” *Phys. Rev. X* **4**, 041011 (2014).
- [20] José Rafael Bordin, Jr. Andrade, José S., Alexandre Diehl, and Marcia C. Barbosa, “Enhanced flow of core-softened fluids through narrow nanotubes,” *J. Chem. Phys.* **140**, 194504 (2014).
- [21] E. R. Smith, “A molecular dynamics simulation of the turbulent couette minimal flow unit,” *Phys. Fluids* **27**, 115105 (2015).
- [22] H. Nowruzzi and H. Ghassemi, “Effects of nano-nozzles cross-sectional geometry on fluid flow: Molecular dynamic simulation,” *J. Mech.* **34**, 667–678 (2018).
- [23] J. Peter Toennies and Andrei F. Vilesov, “Spectroscopy of atoms and molecules in liquid helium,” *Annu. Rev. Phys. Chem.* **49**, 1–41 (1998).
- [24] Giovanni Ciccotti, Raymond Kapral, and Alessandro Sergi, “Non-equilibrium molecular dynamics,” *Handbook of materials modeling*, 745–761 (2005).
- [25] L. J. Garay, J. R. Anglin, J. I. Cirac, and P. Zoller, “Sonic black holes in dilute bose-einstein condensates,” *Phys. Rev. A* **63**, 023611 (2001).
- [26] Jeff Steinhauer, “Measuring the entanglement of analogue hawking radiation by the density-density correlation function,” *Phys. Rev. D* **92**, 024043 (2015).
- [27] Jeff Steinhauer, “Observation of thermal hawking radiation and its entanglement in an analogue black hole,” *Nat. Phys.* **12**, 959 (2016).
- [28] Carlos Barceló, Stefano Liberati, and Matt Visser, “Analogue gravity,” *Living reviews in relativity* **14**, 3 (2011).
- [29] Grant S. Heffelfinger and Frank van Swol, “Diffusion in lennard-jones fluids using dual control volume grand canonical molecular dynamics simulation (dcv-gcmd),” *J. Chem. Phys.* **100**, 7548–7552 (1994).
- [30] Daan Frenkel and Berend Smit, *Understanding molecular simulation: from algorithms to applications*, Vol. 1 (Academic press, 2001).
- [31] Paul L. Barclay and Jennifer R. Lukes, “Mass-flow-rate-controlled fluid flow in nanochannels by particle insertion and deletion,” *Phys. Rev. E* **94**, 063303 (2016).
- [32] Michael Griebel, Thomas Dornseifer, and Tilman Neunhoeffer, *Numerical simulation in fluid dynamics: a practical introduction*, Vol. 3 (Siam, 1997).
- [33] J Karl Johnson, John A Zollweg, and Keith E Gubbins, “The Lennard-Jones equation of state revisited,” *Molecular Physics* **78**, 591–618 (1993).
- [34] Dezső Boda, Tamás Lukács, János Liszi, and István Szalai, “The isochoric-, isobaric-and saturation-heat capacities of the Lennard-Jones fluid from equations of state and Monte Carlo simulations,” *Fluid phase equilibria* **119**, 1–16 (1996).
- [35] Steve Plimpton, “Fast parallel algorithms for short-range molecular dynamics,” *Journal of computational physics* **117**, 1–19 (1995).
- [36] A. P. Thompson, H. M. Aktulga, R. Berger, D. S. Bolin-

- tineanu, W. M. Brown, P. S. Crozier, P. J. in 't Veld, A. Kohlmeyer, S. G. Moore, T. D. Nguyen, R. Shan, M. J. Stevens, J. Tranchida, C. Trott, and S. J. Plimpton, "LAMMPS - a flexible simulation tool for particle-based materials modeling at the atomic, meso, and continuum scales," *Comp. Phys. Comm.* **271**, 108171 (2022).
- [37] Sydney Chapman and Thomas George Cowling, *The mathematical theory of non-uniform gases: an account of the kinetic theory of viscosity, thermal conduction and diffusion in gases* (Cambridge university press, 1970).
- [38] Alauddin Ahmed and Richard J Sadus, "Solid-liquid equilibria and triple points of n-6 Lennard-Jones fluids," *J. Chem. Phys.* **131**, 174504 (2009).